Spectral and morphological properties of quasar hosts in smoothed particle hydrodynamics simulations of active galactic nucleus feeding by mergers

Andrea Cattaneo, Françoise Combes, Stephane Colombi, Emmanuel Bertin, Anne-Laure Melchior

Mon. Not. R. Astron. Soc. **359,** 1237–1249 (2005) doi:10.1111/j.1365-2966.2005.09003.x

Spectral and morphological properties of quasar hosts in smoothed particle hydrodynamics simulations of active galactic nucleus feeding by mergers

A. Cattaneo,[1,2,3★] F. Combes,[4,5] S. Colombi,[3,6] E. Bertin[3] and A.-L. Melchior[4,5,6]

[1]*Institut d'Astrophysique de Paris, 98bis Boulevard Arago, 75014 Paris, France*
[2]*Racah Institute of Physics, The Hebrew University, 91904 Jerusalem, Israel*
[3]*Astrophysikalisches Institut Potsdam, an der Sternwarte 16, 14482, Potsdam, Germany*
[4]*Observatoire de Paris, 61 Avenue de l'Observatoire, 75014 Paris, France*
[5]*Galaxy Formation (GalFor), HORIZON, CNRS, France*
[6]*Numerical Investigations in Cosmology (N.I.C.), HORIZON, CNRS, France*

Accepted 2005 March 8. Received 2005 March 8; in original form 2004 June 9

ABSTRACT

We present a method for generating virtual observations from smoothed particle hydrodynamics simulations. This method includes stellar population synthesis models and the reprocessing of starlight by dust to produce realistic galaxy images. We apply this method and simulate the merging of two identical giant Sa galaxies ($M_{\rm disc} = 10^{11}\,{\rm M}_\odot$, $M_{\rm spheroid} = 2.5 \times 10^{10}\,{\rm M}_\odot$). The merger remnant is an elliptical galaxy ($M_{\rm spheroid} \simeq 1.3 \times 10^{11}\,{\rm M}_\odot$, $M_{\rm disc} \simeq 7.4 \times 10^{10}\,{\rm M}_\odot$). The merger concentrates the gas content of the two galaxies into the nuclear region. The gas that flows into the nuclear region refuels the central black holes of the merging galaxies. We follow the refuelling of the black holes during the merger semi-analytically.

In the simulation presented in this paper, the black holes grow from 3×10^7 to $1.8 \times 10^8\,{\rm M}_\odot$, with a peak active galactic nucleus (AGN) luminosity of $M_B \sim -23.7$. We study how the morphological and spectral properties of the system evolve during the merger, and we work out the predictions of this scenario for the properties of host galaxies during the active phase. The peak of AGN activity coincides with the merging of the two galactic nuclei and occurs at a stage when the remnant looks like a lenticular galaxy. The simulation predicts the formation of a circumnuclear starburst ring/dusty torus with an opening angle of 30°–40° and made of clouds with $n_{\rm H} = 10^{24}\,{\rm cm}^{-2}$. The average optical depth of the torus is quite high, but the obscuring medium is patchy, so that there still exist lines of sight where the AGN is visible in a nearly edge-on view. For the same reason, there are lines of sight where the AGN is completely obscured in the face-on view.

Key words: methods: *N*-body simulations – galaxies: active – galaxies: formation – galaxies: interactions – galaxies: nuclei – quasars: general.

1 INTRODUCTION

Toomre & Toomre (1972) suggested that mergers can convert spiral galaxies into elliptical galaxies. They also remarked that galaxy interactions can determine strong bar instabilities, trigger starbursts and feed gas to active galactic nuclei (AGNs). This paradigm, which links the formation of elliptical galaxies and AGNs to mergers, has derived its strength from its success in smoothed particle hydrodynamics (SPH) simulations of galaxy mergers (e.g. Barnes & Hernquist 1991, 1996; Mihos & Hernquist 1994, 1996) and in semi-analytical models of galaxy formation (e.g. Kauffmann, White & Guiderdoni 1993; Kauffmann & Charlot 1998; Kauffmann & Haehnelt 2000; Cattaneo 2001). The discovery of ultraluminous infrared (IR) galaxies (ULIRGs) with the IR astronomical satellite *IRAS* provided further support for the merger scenario. These galaxies release most of their power in the IR because most of their light is reprocessed by dust. A significant fraction of these objects host AGNs and many are observed to be part of interacting or merging systems (e.g. Bushouse et al. 2002).

Nevertheless, from an observational point of view, the link between AGNs and galaxy interactions is highly controversial. Since the earliest detections of quasar host galaxies with the Canada–France–Hawaii Telescope, there has been a claim that >30 per cent

★E-mail: cattaneo@iap.fr

of quasar hosts are currently interacting with a companion (Hutchings & Campbell 1983). Xilouris & Papadakis (2002) fitted de Vaucouleurs profiles to *Hubble Space Telescope* (*HST*) images of faint AGNs and normal galaxies from the local Universe. After subtracting their fits from the data, they concluded that all active galaxies show significant structure in their inner 100-pc and 1-kpc regions, contrary to quiescent early-type galaxies, which show no structure at all. However, other groups find that the isophotal profiles of quasar hosts are consistent with the de Vaucouleurs law and that their colours are those of old, passively evolving stellar populations, while interactions are no more common than in normal galaxies with similar characteristics (Dunlop et al. 2003).

There is now evidence that AGNs seen through their intense optical/ultraviolet continuum (big blue bump) and broad emission line spectra (type I quasars) are just the tip of the iceberg of the AGN phenomenon (Brandt et al. 2001; Barger et al. 2002; Ueda et al. 2003; Sazonov, Ostriker & Sunyaev 2004) at least in terms of the number of objects. Yu & Tremaine (2002) used the method of Soltan (1982) and Chokshi & Turner (1992) to infer the cosmic density of supermassive black holes due to optical quasars from the quasar luminosity function. They inferred a value of $2.1 \times 10^5\ \mathrm{M}_\odot\ \mathrm{Mpc}^{-3}$, which they compared with their best estimate of the local density of supermassive black holes, $(2.5 \pm 0.4) \times 10^5\ \mathrm{M}_\odot\ \mathrm{Mpc}^{-3}$, concluding that there is limited need for obscured or radiatively inefficient accretion. However, Barger et al. (2005) have shown that extrapolating a fit to the quasar luminosity function outside the measured magnitude range can overestimate the cosmic density due to optical quasars by a factor of 1.75. Moreover, Marconi et al. (2004) disagree with the local density of supermassive black holes estimated by Yu & Tremaine (2002) and propose a value almost twice as large. Unification by orientation (Antonucci & Miller 1985) has proven a successful paradigm to explain the type I/II distinction. In this paradigm, AGNs are surrounded by dusty tori. From a pole-on view, we see the naked AGN and the object is classified as type I. From an equatorial view, the dusty torus obscures the central engine and all we can see is reverberated light/narrow-line emission from clouds illuminated by the AGN. In this case the object is classified as type II.

Studying the host galaxies of type II AGNs is easier because there is not the problem of subtracting the light of the AGN. Nature does it for us. Kauffmann et al. (2003) analysed the spectra of 22 623 narrow-line AGNs from the Sloan Digital Sky Survey. By using the discontinuity at 0.4 μm as an indicator of recent star formation and the strength of the O III 0.5007-μm emission line as an indicator of AGN power, they concluded that low-luminosity AGNs are hosted by normal early-type galaxies. The hosts of bright AGNs are galaxies with the high surface densities of early-type galaxies, but bluer colours indicating recent star formation. They claim that this star formation is not concentrated to the nuclear region. This finding appears to disagree with that of Dunlop et al. (2003) and questions the paradigm of unification by orientation. That is, are the hosts of broad- and narrow-line AGNs drawn from the same population? If starbursts on the scale of the host galaxy contribute to obscure the central engine and the broad-line region, then type I samples may be biased toward AGNs in late-stage or gas-poor mergers.

Here we use numerical simulations (i) to work out the expected properties of quasar hosts in the merging scenario and (ii) to understand the difficulties and selection effects that are present when we try to derive properties of quasar hosts from observations. For this purpose, we run hydrodynamic N-body simulations of galaxy mergers, where we incorporate the effects of absorption by dust and a semi-analytical treatment of the growth of supermassive black holes, interfaced with visualizing tools, which convert the outputs of the simulations into mock data (including instrumental diffraction, sky noise, etc.)

The hydrodynamic simulations use the three-component (stars, gas and dark matter) SPH tree code GALMER (Combes & Melchior 2002) described in Section 2. The modelling of the stellar spectral energy distribution (SED) and of the reprocessing of starlight by dust is performed after the simulations, through an interface that manipulates the outputs of the simulations (Section 3). The same is true for the growth of the central black hole, which is computed semi-analytically from the rate at which gas falls into the central 100 pc.

In Section 5 we present the results of our analysis of the outputs of the simulation. In this analysis, we concentrate on three questions: (i) the relation between the global star formation history of the host galaxy and star formation/black hole accretion in the galactic nucleus; (ii) the relation between the spectro-morphological evolution of the host galaxy and the growth of the central black hole; (iii) the geometry, the optical depth and the covering factors of the absorbing materials. In Section 6, we summarize the main new results of this work.

This paper is part of a project to build a library of simulated galaxy mergers. Here, we only consider one simulation where we merge two identical Sa galaxies. In a future publication, we shall discuss how the results of this paper depend on the merging parameters and on the properties of the merging galaxies.

2 HYDRODYNAMIC SIMULATIONS

2.1 GALMER SPH code

Gravitational hydrodynamics is simulated with the GALMER SPH tree code, which is a development of the code used by Combes & Melchior (2002). In GALMER, galaxies are composed of three types of particles: stellar particles, dark matter particles and hybrid particles. At the beginning of a simulation, a hybrid particle is made entirely of gas. We assume that the gas is isothermal and cools very efficiently. We calculate pressure forces for an isothermal gas with a temperature of 10 000 K. This is approximately the temperature where there is strong change in the cooling curves (Blumenthal et al. 1984). The adopted star formation rate is given by the modified Schmidt law

$$\dot{\rho}_* = 8.33 \times 10^7\ \mathrm{M}_\odot\ \mathrm{kpc}^{-3}\ \mathrm{Myr}^{-1} \times \left(\frac{\rho_\mathrm{g}}{10^9\ \mathrm{M}_\odot\ \mathrm{kpc}^{-3}}\right)^{1.2} \left(\frac{\sigma}{100\ \mathrm{km\ s}^{-1}}\right)^{\eta}, \quad (1)$$

where ρ_g is the density of the gas and σ is the local velocity dispersion of the hybrid particles. We take $\eta = 1.5$ for regions where the divergence is negative and the gas is shocked, while we take $\eta = 0$ for regions where the gas is expanding. When the gas content of a hybrid particle drops below 5 per cent, the hybrid particle is turned into a stellar particle and its gas content is spread among the neighbouring hybrid particles. It is useful to think of a hybrid particle as a model for a giant molecular cloud, which evolves into a star cluster once all the gas has been locked into stars.

2.2 Initial conditions for the merging galaxies

In this first paper, we concentrate on the results of one simulation, in which we merge two identical galaxies. Each of the two galaxies is made of four components: the dark matter halo (dark matter

Table 1. Initial galaxy parameters in the SPH simulation.

Component	M ($M_\odot$)	N_p	a (kpc)	b (kpc)
DM halo	1.25×10^{11}	40 000	0	50
Stellar disc	1.00×10^{11}	48 000	4	0.5
Gas disc	1.00×10^{10}	20 000	5	0.2
Bulge	2.50×10^{10}	12 000	0	2

particles), the stellar disc (stellar particles), the gas disc (hybrid particles) and the bulge (stellar particles). Each of the four components is a random realization of a Miyamoto–Nagai density profile (Miyamoto & Nagai 1975), which, in cylindrical coordinates r, ϕ, z, takes the form

$$\rho(r,z) = \frac{b^2 M}{4\pi} \frac{ar^2 + [a + 3(z^2+b^2)^{1/2}][a + (z^2+b^2)^{1/2}]^2}{\{r^2 + [a + (z^2+b^2)^{1/2}]^2\}^{5/2}(z^2+b^2)^{3/2}}. \quad (2)$$

M is the total mass of the component, while a and b are two characteristic length-scales. The Miyamoto–Nagai density distribution tends to a Plummer sphere with radius b in the limit $a \to 0$ and to a Kuzmin disc with radius a in the limit $b \to 0$. These density distributions are discussed at length in the textbook by Binney & Tremaine (1987). Table 1 gives the mass M, the number of particles N_p and the characteristic scalelengths a and b for each of the four components. The masses and the numbers of particles that are given in Table 1 are the values for one galaxy. The total number of particles is 240 000.

2.3 SPH outputs

We save the outputs of the SPH simulations at intervals of 25 Myr. The five snapshots in Figs 1 and 2 convey an idea of the merging dynamics. Soon after the simulation has started, the discs become unstable in the bar mode. The bars in the gas discs are stronger than the bars in the stellar discs and are accompanied by more violent inflows along the bar direction.

The galaxy labelled galaxy 1 is the one that is above in the 100-Myr snapshot and below in the 200-Myr snapshot (Fig. 1). The two galaxies are identical, but it is to this one that we refer when we give information pertaining to one galaxy only (zoom, central star formation, etc.).

3 FROM SPH SIMULATIONS TO MOCK ASTRONOMICAL DATA

3.1 Modelling stellar colours with PEGASE

Given an initial stellar mass function (for us, a Salpeter initial mass function), the colours of a stellar population are a function of how old its stars are. We can reconstruct the colours of the hybrid particles by tracking how the gas content of each particle varies at each 25 Myr. In this way we can decompose the stars of hybrid particles into those which formed in the last 25 Myr, those which have an age $25 < t_* < 50$ Myr, and so on. If we assume that the star formation rate is uniform over intervals of 25 Myr, then we can reconstruct the colours of the hybrid particle with the PEGASE stellar spectral evolution model (Fioc & Rocca-Volmerange 1997). Because we only saved snapshots at intervals of 25 Myr, we lack the time resolution to see nebular lines. This is a purely technical limitation dictated by the memory of the workstation and is easily overcome. Moreover, it has no consequence for the results of this paper.

It is more difficult to determine the colours of the stellar populations that pre-existed the beginning of the simulation. For bulge stars we just assume a uniform age of 8 Gyr at the start. For the stellar disc we follow the method described by Segalovitz (1975). In his model the gas disc was assembled 10 Gyr ago with no further growth from later gas cooling on to the disc. The gas is in differential rotation and, owing to secular instabilities, the disc very rapidly develops spiral arms. Each time a gas cloud passes through a spiral arm, a fraction p of the gas goes into stars and is not returned to the interstellar medium again. In this model the gas surface density evolves as $\Sigma_{\rm gas}(r,t) = \Sigma_{\rm gas}(r,0)\exp(-\beta t)$. Here $\beta \equiv (2\pi)^{-1} n(\Omega - \Omega_p)p$, where n is the number of spiral arms, $\Omega(r)$ is the rotation angular velocity required to support the disc and Ω_p is the pattern angular velocity of the spiral arms. Searle, Sargent & Bagnuolo (1973) determined the colours for a stellar population, the formation of which started 10 Gyr ago and continued from then onward at an exponentially decaying rate on a time-scale β^{-1}. Segalovitz (1975) used their determination of B–V as a function of β together with the data on B–V as a function of galactocentric radius then available for M81. In this way he was able to reconstruct $\beta(r)$. He found a good fit to the data for $p \simeq 0.2$ and $\Omega_p \ll \Omega$. Here we use his model with $n = 2$, $\Omega_p = 0$ and $p = 0.2$ to compute $\beta(r)$ for the discs of our model galaxies. $\Omega(r)$ is given by the analytical formula for a Miyamoto–Nagai density distribution (Miyamoto & Nagai 1975). This scheme assigns an r-dependent age to each of the particles composing the stellar disc. PEGASE is then used to calculate the magnitudes of these particles. After 10 Gyr, we expect a higher gas fraction in the outer parts of the disc, where matter has had time to complete fewer galactic rotations. We model this effect by attributing two different scale radii to the gas disc and the stellar disc (Table 1).

Reality is more complicated because (i) the transformation of gas into stars is accompanied by an evolution in the dynamic and kinematic structure of the disc, (ii) star formation is inevitably accompanied by stellar feedback, and (iii) the outskirts of the disc will accrete fresh gas from the surrounding environment. However, the purpose of the model described here is simply to generate plausible initial conditions for the colours of the merging galaxies, and this simple model accomplishes this task quite well.

3.2 Dust absorption / emission

The reprocessing of starlight by dust is computed with the STARDUST model (Devriendt, Guiderdoni & Sadat 1999). The optical extinction scales linearly with the column of neutral hydrogen on the line of sight and with the metallicity of the obscuring material. For a neutral hydrogen column density on the line of sight of $n_{\rm H} = 10^{20}$ cm^{-2} and solar abundances, the R-, V- and B-band extinctions are $A_R \simeq 0.040$ mag, $A_V \simeq 0.049$ mag and $A_B = 0.062$ mag. The chemical evolution of the interstellar medium is already included in the hydrodynamic code, while $n_{\rm H}$ is determined in the phase of post-processing, because it depends on the viewing angle. All hybrid particles in front of a hybrid or stellar particle contribute towards absorbing the light of that particle. Moreover, in the case of hybrid particles, there is also a contribution from self-absorption.

The main difficulty derives from the fact that the SPH simulation cannot resolve the gas clouds that produce the absorption. Hybrid particles correspond to gas clouds of 10^4 to 5×10^5 $M_\odot$, which is the appropriate mass range for large molecular clouds. If the absorption of light was uniform over a cloud's entire cross-section, then a cloud radius of $r_{\rm cloud}$ would correspond to $n_{\rm H} \simeq 1.3 \times 10^{21} (M_{\rm cloud}/10^5\,M_\odot)\,(r_{\rm cloud}/50\,{\rm pc})^{-2}$ (assuming that

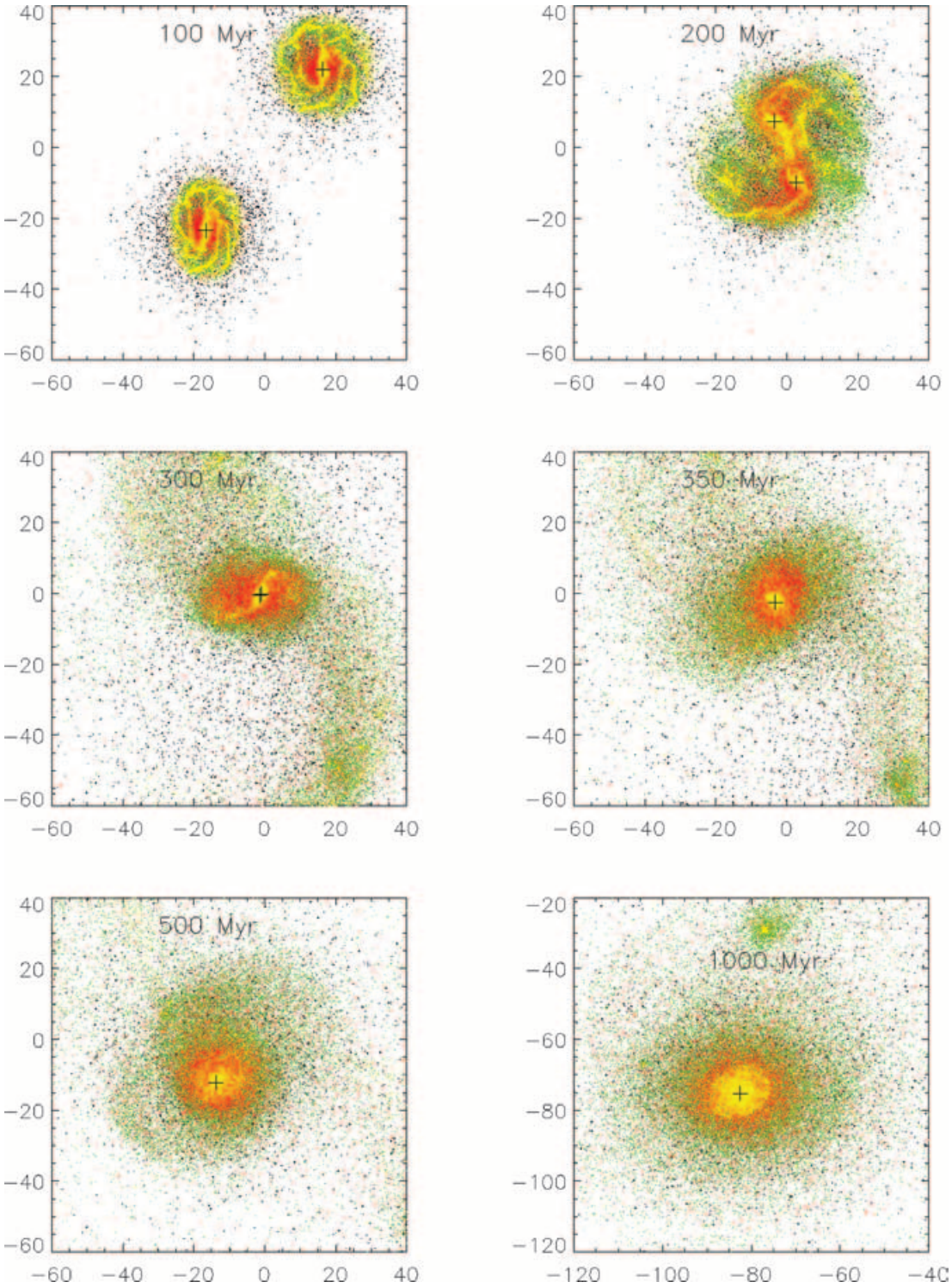

Figure 1. A sequence of five snapshots from the GALMER SPH simulation. The time elapsed from the beginning of the simulation is printed on each snapshot. The units on the axis are kpc. Black is dark matter, green is old disc stars, red is bulge stars and yellow is gas/young stars.

80 per cent of the cloud mass $M_{\rm cloud}$ is composed of hydrogen). However, in reality, molecular clouds do not absorb light uniformly because the cold gas has a fractal distribution. Large clouds are composed of smaller clouds interspersed with voids. Furthermore, the concept itself of associating hybrid particles with large molecular clouds is qualitatively useful but is dangerous when used quantitatively because only smoothed quantities can be relied on to represent physical properties.

The more sensible approach is to compute a smoothed $\langle n_{\rm H}\rangle$ for the gas in front of each particle and then to use this $\langle n_{\rm H}\rangle$ together with assumptions about the physical properties of the obscuring clouds in order to generate a Monte Carlo $n_{\rm H}$. It is this second $n_{\rm H}$ that we

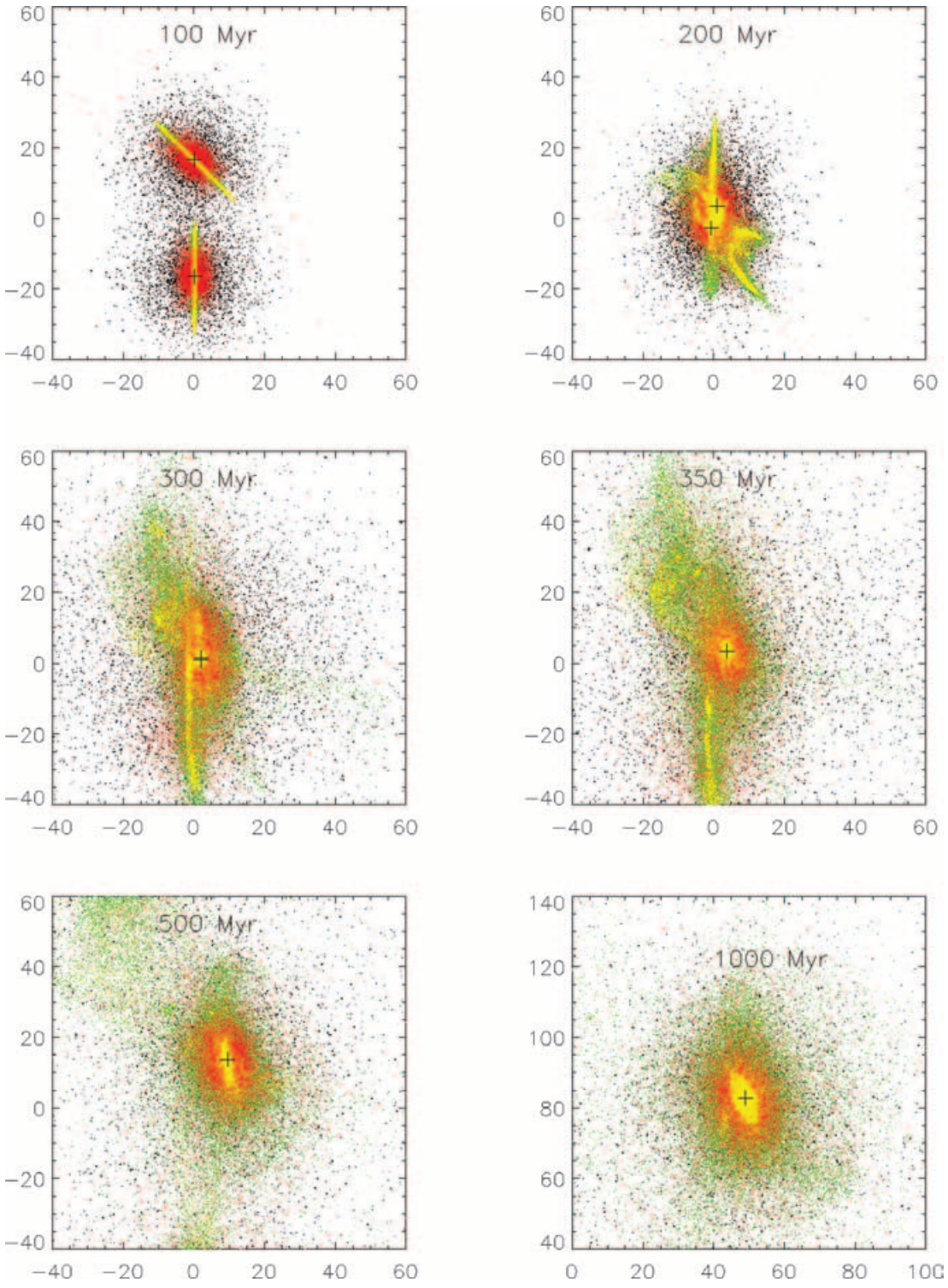

Figure 2. The same as in Fig. 1 from an orthogonal viewing angle.

eventually use to calculate the optical extinction. To pass from $\langle n_{\rm H}\rangle$ to a probability distribution for $n_{\rm H}$ we need to make some hypothesis about the column densities of the clouds that produce the extinction. In reality, the distribution of cloud properties is very broad, but here we simply assume that all clouds have the same column density $n_{\rm H}^{\rm cl}$. If $\langle n_{\rm H}\rangle \ll n_{\rm H}^{\rm cl}$, then in most cases there will be no cloud or one cloud at most on the line of sight. The probability of the second occurrence is therefore $\sim\langle n_{\rm H}\rangle/n_{\rm H}^{\rm cl}$. If $\langle n_{\rm H}\rangle \gg n_{\rm H}^{\rm cl}$, then typically there will be a number of $\sim\langle n_{\rm H}\rangle/n_{\rm H}^{\rm cl}$ clouds on the line of sight, and we can expect deviations from the average extinction to be small if this number is large.

STARDUST is used to compute the bolometric luminosity absorbed over the entire optical spectrum. This power is returned in the IR as thermal dust emission with a modified blackbody spectrum. A

modified blackbody describes the physical reality better than the Planck formula because the dust is transparent to photons at wavelengths $\gg$200 μm, so that radiation in that part of the spectrum is no longer thermalized.

When we compute broad-band IR spectra for the whole galaxy, we do not consider absorption and emission by individual clouds. Instead, we compute a smoothed $n_{\rm H}$ map, where one pixel corresponds to $100 \times 100\,{\rm pc}^2$. We also compute $\bar{z}_* \pm \Delta z_*$ and $\bar{z}_{\rm gas} \pm \Delta z_{\rm gas}$ at each pixel for the distribution of stellar and hybrid particles along the line of sight (z is the Cartesian coordinate in the direction of the line of sight, not to be confused with the metallicity Z). We use the results of these calculations to determine the surface brightness that is absorbed and re-emitted. This is how we calculate the IR emission from dust heated by starlight.

We also calculate IR spectra when the AGN contributes towards heating the dust. We shall see later on that in our simulation ∼80 per cent of the lines of sight looking towards the central engine are obscured. The obscured lines of sight have optical depth $\tau \gg 1$ (see the $n_{\rm H}$ column in Table 2). The absorbed power is therefore an important fraction of the AGN's bolometric luminosity. Therefore, we can make the approximation that there is an optically thick central region, which absorbs ∼80 per cent of the AGN power and re-emits it with the modified blackbody spectrum described above. The radius of the self-absorbed central region gives the characteristic radius of the surface that re-emits the absorbed AGN light. We compute this radius to estimate the temperature of the re-emitted radiation.

Table 2. Virtual observations of the AGN at different viewing angles.

θ (°)	$\langle N_{\rm H}\rangle$ (10^{24} cm^{-2})	$Z/Z_\odot$	M_B (AGN)
0	0.196349	1.89471	−23.7
3	0.294102	1.49658	−23.7
6	0.292391	1.81359	−23.7
9	0.287282	1.71863	376
12	0.216616	1.89728	−23.7
15	0.155719	2.10944	−23.7
18	0.166973	1.74387	376
21	0.478099	1.32532	−23.7
24	0.339831	1.37435	−23.7
27	0.340767	1.75315	376
30	0.329107	1.59405	376
33	0.361234	1.54440	376
36	0.599168	1.60186	376
39	0.359224	1.65867	−23.7
42	1.14970	1.64893	735
45	0.351887	1.81494	376
48	0.769909	1.77040	521
51	0.0939574	1.72862	−23.7
54	0.666031	1.92951	490
57	0.581031	1.75790	385
60	0.505869	1.63132	376
63	0.693351	1.67498	441
66	0.436236	1.64965	−23.7
69	0.640693	1.72126	417
72	1.59603	1.86413	1166
75	1.06212	2.01813	834
78	0.879192	1.78262	603
81	0.997245	2.03174	787
84	1.00148	1.66960	645
87	1.05674	1.80867	741
90	1.45602	1.81765	1035

3.2.1 Creating mock images

The software package SKYMAKER (http://terapix.iap.fr/soft) is used to convert the projected coordinates and extinction-corrected magnitudes of the simulated particles into mock images in the Johnson *B*, Johnson *V* and Cousins *R* bands. These images are generated as files in the .FITS format. Therefore, it is possible to perform on them all the manipulations that could be performed on real data. SKYMAKER can model instrumental diffraction, photon noise and atmospheric blurring. Because it is possible to put the galaxies at an arbitrary distance, this technology can be used not only to explore theoretical scenarios for galaxies and AGNs, but also to assist the development of new observing proposal by determining in advance which features would be observable at a given flux limit or under certain sky conditions (in the case of ground-based telescopes).

Fig. 3 shows a true colour image of one of the two galaxies before the merger takes place. This snapshot is generated by using the *RVB* colour system to superimpose images in the *B*, *V* and *R* bands. This image shows the dust lane cutting through the galactic disc.

4 THE BLACK HOLE

4.1 The approach

We assume that the two galaxies start with central black holes of $3 \times 10^7\,{\rm M}_\odot$. This mass is inferred from the black hole mass to bulge mass relation in Häring & Rix (2004).

The mass resolution of the simulation is not sufficient to compute the orbits of the black holes correctly because, while in reality the black hole mass is much larger than the stellar mass, so that the black holes sink to the centre due to dynamical friction, this is not the case in our simulation. Therefore, we impose as a constraint that the black hole is in the galactic nucleus at all times and we calculate the accretion rate from the fuel supply that is present in the nuclear region. This approach relies on a correct identification the galactic centre.

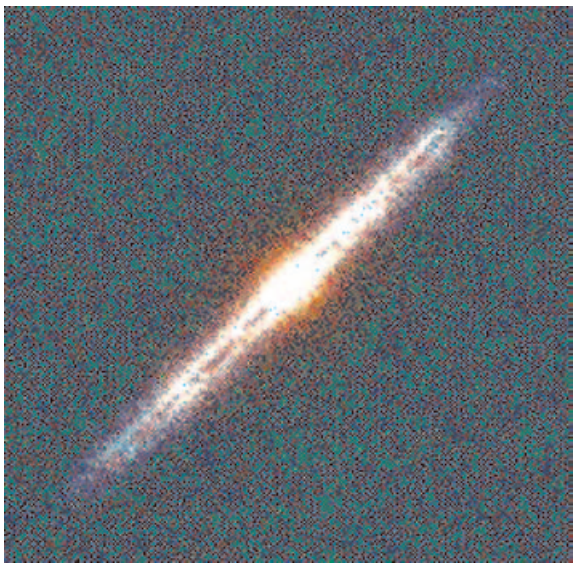

Figure 3. A close-up image of galaxy 1 viewed edge-on shows the central dust lane.

4.2 Identifying the galactic centre

The identification of density peaks in the simulation outputs is performed with the substructure finder ADAPTAHOP, described in detail in Aubert, Pichon & Colombi (2004). Basically, this algorithm applies SPH smoothing to the particle distribution, then finds local density maxima and saddle points in this smoothed distribution and constructs a tree of structures and substructures by using the value of the density at saddle points to control connectivity between various subcomponents of the system. The local maxima correspond to the leaves of the tree. A given substructure is identified as the set of particles verifying $\rho_{\rm SPH} \geqslant \rho_{\rm saddle}$, where $\rho_{\rm SPH}$ is the SPH density associated with each particle and $\rho_{\rm saddle}$ is the value of the SPH density at the (highest) saddle point connecting this substructure to its neighbour. The output of ADAPTAHOP depends on the choice of various parameters, namely the number $N_{\rm SPH}$ of particles used to perform SPH smoothing, the number $N_{\rm HOP}$ of neighbours used to walk into the particle distribution in order to find local maxima and to establish connectivity through saddle points, and a parameter $f_{\rm Poisson}$ controlling the significance of substructures compared to Poisson noise. Our choices for these parameters are those advocated in Aubert et al. (2004), namely $N_{\rm SPH} = 64$, $N_{\rm HOP} = 16$ and $f_{\rm Poisson} = 4$, the latter value meaning that only substructures at the 4σ level compared to pure Poisson noise are considered as real. Besides these parameters, there is also an overall density threshold, $\rho_{\rm TH}$, which is used to eliminate all particles with SPH density below $\rho_{\rm TH}$ prior to the analysis. This we set here to a very small value (in cosmological simulations, $\rho_{\rm TH}$ controls the selection of dark matter haloes).

In ADAPTAHOP, a galaxy is thus viewed as a tree, which separates into several branches, which separate into smaller branches, which separate into leaves, corresponding to small-scale density peaks. This tree represents how smaller structures are nested into larger structures through saddle points at a fixed time, and has nothing to do with merger trees encountered in cosmological simulations of galaxy formation. We search for density peaks in the leaves of the tree by starting from the leaves that contain the highest masses. This usually gives a good identification of the galactic nucleus. Instead, by starting from the leaves with the highest density one often misses the galactic nucleus and finds molecular clouds in the spiral arms. One can look at Fig. 1 and see that the centres identified by this automatic procedure, marked by little black crosses, are, as they should be, at the centres of the two galaxies. Identifications are made secure by the fact that the galactic nucleus is not just a name for the central region, but stands out as a well-defined dynamical entity (see the right-hand column of Fig. 5). Moreover, we have verified that the particles which are in the galactic nucleus (identified as the region at a radius of $r < 100$ pc) at the beginning of the simulation, remain in the galactic nucleus during the entire simulation. A small fraction are stripped from the galactic nucleus in mini-tidal tails, but they eventually fall back into it.

4.3 Fuelling the central black hole by orbital decay of large molecular clouds

Our SPH simulation can follow the inflow of gas from a few kpc into the central 100 pc, but lacks the resolution to follow the inflow of gas from a 100-pc distance into the central black hole. Following Shlosman & Noguchi (1993), we imagine that the stream of matter from the galactic nucleus into the black hole is due to the orbital decay of giant molecular clouds, which are subject to the dynamical friction of stars and of lower-mass clouds and which are eventually disrupted by tidal forces. At that point the clouds are stretched into a continuous accretion flow into the black hole. The formula for the accretion rate from the orbital decay of molecular cloud is

$$\dot{M}_\bullet = 2 \times 10^{-3} \frac{\psi}{0.1} \frac{M_{\rm cloud}}{10^5\,{\rm M}_\odot} \frac{M_{\rm gas}}{10^9\,{\rm M}_\odot} \frac{\rho_*}{{\rm M}_\odot\,{\rm pc}^{-3}} \times \frac{v_{\rm a}}{10\,{\rm km\,s}^{-1}} \left(\frac{v_{\rm c}}{100\,{\rm km\,s}^{-1}}\right)^{-1} \left(\frac{\sigma_*}{25\,{\rm km\,s}^{-1}}\right)^{-3} \frac{{\rm M}_\odot}{\rm yr} \quad (3)$$

(Shlosman & Noguchi 1993), where ψ is the fraction of the total gas in the galactic nucleus $M_{\rm gas}$ that is contained in clouds of mass $> M_{\rm cloud}$, ρ_* is the stellar density in the galactic nucleus, σ_* is the stellar velocity dispersion, $v_{\rm a}$ is the relative velocity at which the gas rotates with respect to the stars and $v_{\rm c}$ is the rotational velocity of the gas. We extract all these quantities directly from the outputs of the SPH simulation and use them to compute $\dot{M}_\bullet$. The two black holes merge when we can no longer separate the nuclei of the two galaxies. The reader should be warned that the precise value and evolution of $\dot{M}_\bullet(t)$ is sensitive to the details of how we calculate the average quantities mentioned above, but we have verified that none of our conclusions depends on these details. Moreover, our model for the black hole accretion rate tends to smooth the accretion rate over time. The real pattern of black hole accretion is more likely to be a sequence of bursts with variability on all time-scales. The most pragmatic approach to deal with this reality when necessary is to introduce an AGN duty cycle, so that the quasar is only active for a fraction of the simulation time. The accretion rate during the active phase is correspondingly increased to account for the presence of this duty cycle.

5 RESULTS

The evolution of the system during the merger is shown by the sequence of snapshots in Figs 4 and 5. For each of the four represented time-steps, which correspond to 100, 200, 300 and 350 Myr from the beginning of the simulation, we show an 80×80 kpc^2 face-on image (Fig. 4, left column), an 80×80 kpc^2 edge-on image (Fig. 4, right column), an 80×80 kpc^2 face-on image, where we only show the unextinguished young stellar population (the light coming from hybrid particles; Fig. 5, left column), and a 2×2 kpc^2 zoom of the nuclear region of galaxy 1 (Fig. 5, right column). See the end of Section 2 for an explanation of which one is galaxy 1. Enlarged images of the central region are taken from face-on images. Compare these images with Figs 1 and 2 and notice that SKYMAKER reverses the original images.

On a large scale, the two galaxies are merging in a dynamical time. Their relative orbit reaches a point of closest approach and has only time to make a turn before the galaxies merge owing to dynamical friction. On a small scale, inside each galaxy, the tidal forces trigger matter inflow. This process culminates with the merger of the two nuclei, which occurs about 50 Myr after the galaxies as a whole have merged, and ends with a stream of debris that keeps on falling into the nuclear region during the post-merger phase of dynamical relaxation.

5.1 Star-forming regions

The most obvious result coming out of these images is that strong star formation is concentrated in a series of knots along gas spiral arms, which are much more pronounced and filamentary than the spiral arms in the stellar disc. The galactic nucleus stands out as the central one and the most prominent of these knots. As the simulation progresses, these knots, associated with the formation of massive star clusters, fall to the centre and merge with the galactic nucleus.

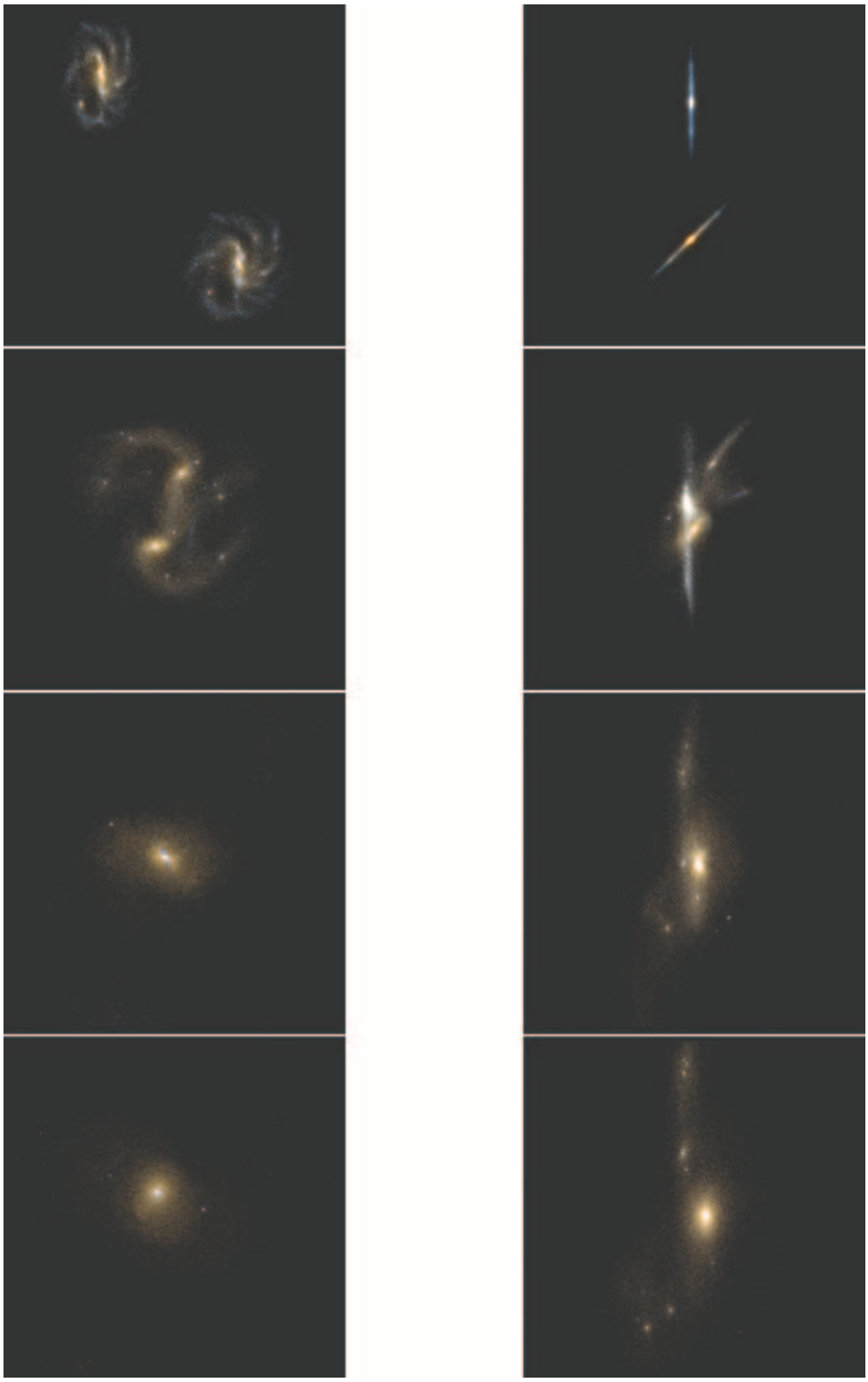

Figure 4. Face-on (left column) and edge-on (right column) snapshots of the merging process. From top to bottom, the snapshots were taken 100, 200, 300 and 350 Myr after the simulation started. The snapshots were generated with the SKYMAKER software by superimposing *B*-, *V*- and *R*-band images. Each image corresponds to a square of 80 kpc side.

The star formation rate in the host galaxy is a good tracer of the star formation rate in the nuclear region (Fig. 6). For this reason, we do not find evidence for a delay between star formation in the host galaxy and supply of fuel to the central region.

The first peak of star formation in Fig. 6 is exaggerated by the artificial assumption that the discs are initially axisymmetric (Fig. 7). The assumed initial condition is highly unstable. The first peak of star formation would have been absent if we had started from a

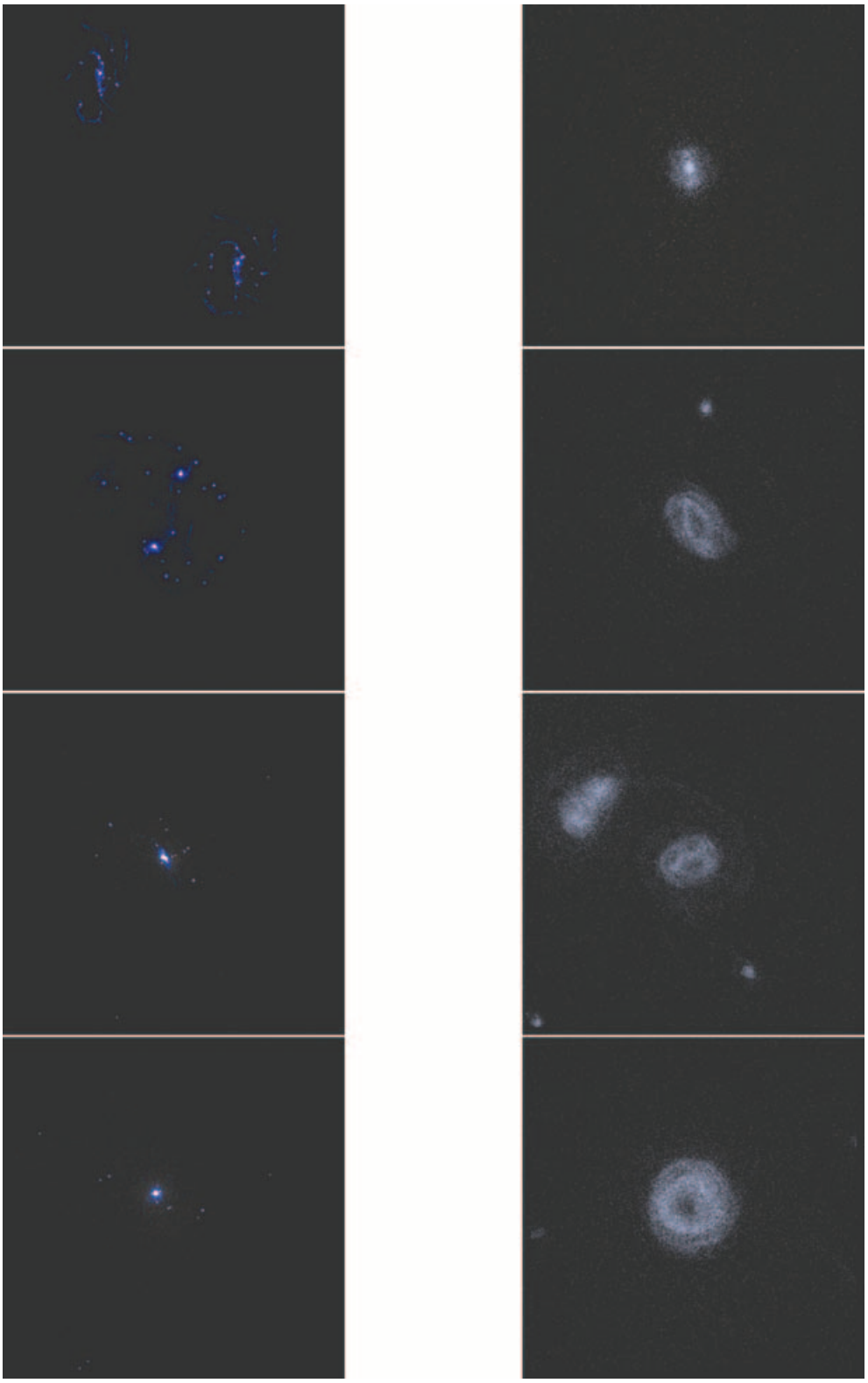

Figure 5. The left column corresponds to left column of Fig. 4 with the difference that here we only show the young stellar population formed after the simulation began. In these four snapshots, and in these four snapshots only, we have neglected the extinction of starlight by dust. The right column shows a 2×2 kpc^2 zoom of the nucleus of galaxy 1. These snapshots were derived by zooming into the images in the left column of Fig. 4. Young stars dominate the emission.

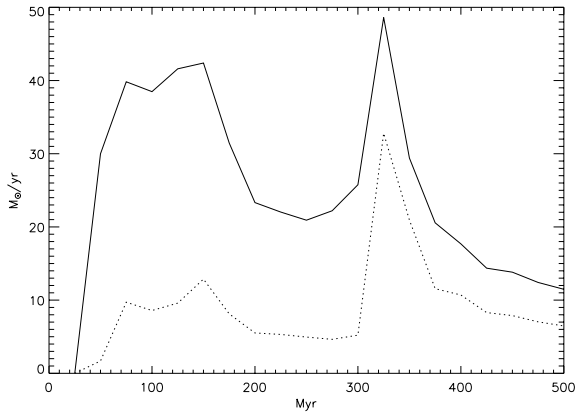

Figure 6. The global star formation rate in the merging system (solid line) compared to the star formation rate in the nucleus of galaxy 1 (dotted line).

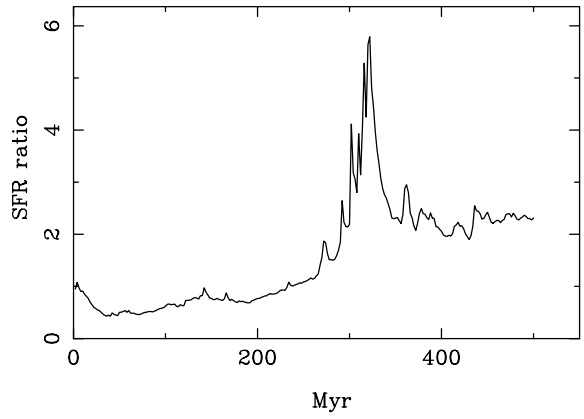

Figure 7. Ratio between star formation rate in the merger simulation and star formation rate for an isolated galaxy as a function of time.

relaxed dynamical configuration. The second peak corresponds to a physical phenomenon, the starburst triggered by the merger. During this starburst, the star formation rate is about six times higher than it is in an isolated galaxy.

5.2 The dusty torus

The second important finding is the formation of a nuclear starburst ring or dusty torus at the galactic centre. The large number of particles in the central 300 pc combined with the use of a tree code enable us to obtain a higher resolution in the central region. We have estimated that, even under the most disfavourable assumptions, our resolution limit in the central region is smaller than 40 pc. Therefore, we are confident to resolve the hydrodynamics of the central 300-pc region, from the mean properties of which we calculate the black hole accretion rate semi-analytically (equation 3). The torus in Fig. 5 has an inner radius of ∼40 pc and an outer radius ∼250 pc with most of the mass at ∼130 pc. The mass-averaged rotation speed and the one-dimensional velocity dispersion within a distance $r_{\rm max} = 250$ pc from the centre of the remnant are $v_{\rm rot} = 140$ km s^{-1} and $\sigma = 63$ km s^{-1}, respectively. We have verified that $v_{\rm rot}^2 \simeq GM(r_{\rm max})/r_{\rm max}$, where $M(r_{\rm max})$ is the mass at $r < r_{\rm max}$ and G is the gravitational constant, which means that the torus is supported by rotation. The ratio between the thickness and the diameter of the torus is consistent with the $\sigma/v_{\rm rot}$ ratio. The formation of a central starburst ring such as that described in this paper has already been reported by Heller & Shlosman (1994). They simulated the dynamical evolution of globally unstable galactic discs and discussed how supernova explosions, radiation-driven winds from massive stars and the presence of supermassive black holes affect the dynamical evolution of the starburst ring. Our simulation does not model these effects, which may play an important role in the evolution of the central region. We observe the formation of a well-defined torus after the nuclei of the two galaxies have merged, but after ∼50 Myr the torus is no longer recognizable in an obvious manner. At that point, the structure of the galactic nucleus changes from a torus into a mini-spiral with asymmetric spiral arms as more gas and stars fall into the central region. Less obvious tori are also seen before the two nuclei merge.

The nuclear region is very dusty. We have assumed that the torus is made of clouds with $n_{\rm H}^{\rm cl} = 10^{24}$ cm^{-2} (like the Orion nebula) and we have conducted virtual observations of the AGN 350 Myr after the simulation began. We have observed the AGN at inclination angles from pole-on ($\theta = 0^\circ$) to edge-on ($\theta = 90^\circ$). The azimuthal angle ϕ was selected randomly at each observation. In Table 2 we give the results of this Monte Carlo experiment showing the smoothed column density $\langle n_{\rm H}\rangle$ and the extinguished AGN blue magnitude M_B for each observation. $M_B = -23.7$ is the absolute blue magnitude of the unobscured AGN and $M_B = 376$ corresponds to one cloud on the line of sight.

The average column density of neutral hydrogen on the line of sight to the AGN is fairly high at all viewing angles and grows by an order of magnitude when we pass from a pole-on to an edge-on view. If the dusty torus is composed of clouds with high optical depth, then the AGN appears as a Seyfert 1 when it is observed pole-on and as a Seyfert 2 when it is observed edge-on. Table 2 shows that there are a few exceptions to this rule due to the presence of clouds in the polar regions and holes in the dusty torus. Table 2 also shows that the metallicity of the dusty torus is about twice the solar value due to intense star formation activity in the torus.

5.3 Quasar hosts

Quasar host galaxies have been investigated according to both morphological and spectral criteria. We have analysed the morphology of the merger remnant by using IRAF to fit elliptical isophotes to *R*-band mock images. We compared the photometric profiles extracted by this procedure with de Vaucouleurs and exponential disc profiles. We repeated the same analysis by using mass surface density profiles determined by computing the surface density in circular coronae around the galactic centre. Both methods gave similar results in terms of the bulge/disc decomposition. Fig. 8 shows how the surface density profile evolved from $t = 100$ Myr to $t = 500$ Myr. We see a transition from a more exponential disc-type to a more de Vaucouleurs-type profile. In Fig. 9 we show a spheroid plus disc decomposition of the surface density profile at 500 Myr. This decomposition corresponds to $M_{\rm spheroid} = 1.34 \times 10^{11}$ M$_\odot$ and $M_{\rm disc} = 7.4 \times 10^{10}$ M$_\odot$. Fig. 10 shows how the merger remnant would appear in an *HST* image if it was at a redshift of 0.27 and was photographed with the Wide Field Camera mounted with the 814-μm filter. The AGN is visible and has a luminosity of $M_B = -22$. We clearly see two tails of debris falling on the merger remnant from opposite directions.

Fig. 11 shows how the optical and IR spectra evolve during the merger. The solid lines show the total spectrum while the dashed lines show the spectrum without the AGN. The optical spectrum is produced by direct light from stars and from the AGN. The

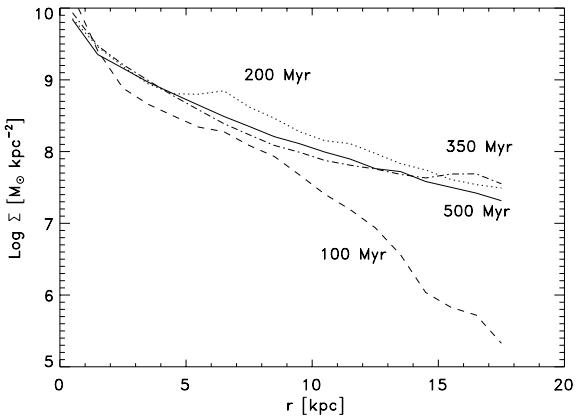

Figure 8. Surface density profile of the first galaxy 100 Myr (dashed line), 200 Myr (dotted line), 350 Myr (dashed-dotted line) and 500 Myr (solid line) after the simulation has started.

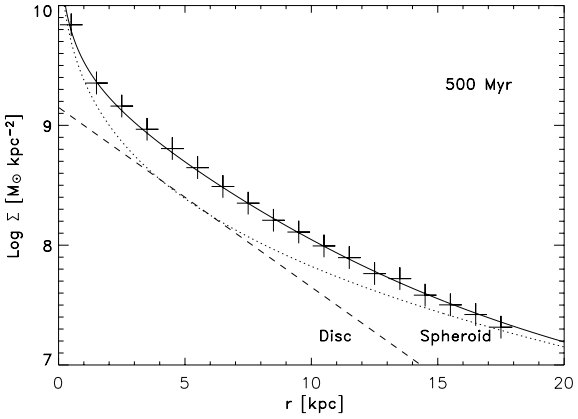

Figure 9. Surface density profile of the merger remnant 500 Myr after the simulation has started (crosses). The solid line fit is the sum of a de Vaucouleurs profile $\propto \exp[-(r/r_{\rm e})^{1/4}]$ (dotted line) and an exponential disc $\propto \exp(-r/r_{\rm d})$ (dashed line). The fit shown on this diagram corresponds to $M_{\rm spheroid} = 1.34 \times 10^{11}$ M$_\odot$, $M_{\rm disc} = 7.4 \times 10^{10}$ M$_\odot$.

IR/submm spectrum is produced by thermal dust heated by stars and by the AGN. The AGN contributes to the IR and submm emission independently of the viewing angle because most of the AGN power is absorbed and thermalized whether the clouds are on the line of sight or not (e.g. Sazonov et al. 2004). On the other hand, the direct optical emission from the AGN is totally extinguished in most cases.

In Fig. 11, the *B* band corresponds to $\mathrm{Log}(\lambda/\mu\mathrm{m}) \simeq -0.37$. At all times, the most important contribution to the optical spectrum comes from the old stellar population pre-existing the merger, not only because most of the stellar mass is in old stars, but also because young stars are heavily obscured by dust. However, as the merger progresses, clear signals of star-forming activity emerge from the IR and ultraviolet parts of the spectrum. The presence of an AGN raises the IR flux substantially by increasing the temperature of the dust in the central starburst ring from 43 to 63 K.

6 DISCUSSION AND CONCLUSION

We have developed a tool that can simulate real galaxy images to a very high degree of realism. Our study confirms the powerful effect of mergers on galactic morphologies and the accumulation of cold gas in the galactic centre that were seen in previous studies (e.g. Barnes & Hernquist 1996; Mihos & Hernquist 1996). The gas that concentrates in the galactic centre forms a starburst ring, which can fuel an AGN. Heller & Shlosman (1994) have already encountered this configuration in SPH simulations of globally unstable isolated disc galaxies. They have made simulations with and without supernova feedback. Without feedback, gas has a much stronger tendency to fragment into a few large clumps, but the effect on the final black hole mass is not significant. We are aware that we lack the resolution to investigate the distribution of gas in the starburst ring and the black hole accretion rate from the SPH simulation, although our resolution length is at least three times smaller than the characteristic radius of the torus. Instead, we study these aspects by applying a semi-analytical treatment to the outputs of the simulation.

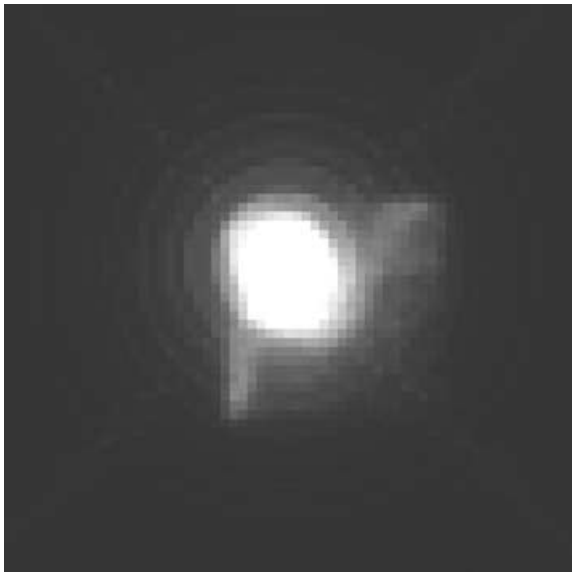

Figure 10. Mock *HST* image of the system 500 Myr after the simulation has started. The system is assumed to be at $z = 0.27$ and is observed at a viewing angle from which it is possible to see the central engine; hence the diffraction rings. The imaging model mimics the 814-μm filter on the Wide Field Camera.

Even under conservative assumptions for the fuelling rate, the accretion of gas increases the black hole mass by a factor of $\gtrsim$3. Another factor of 2 is gained by merging the two black holes, so that the black hole starts with a mass of 3×10^7 M$_\odot$ and reaches a mass of $\sim 1.8 \times 10^7$ M$_\odot$ by the end of the simulation. We have simulated a relatively gas-poor merger. The starburst would be much stronger if the discs had a higher gas fraction; so would the growth of the central black hole.

This increase in black hole mass is comparable to the increase in bulge mass from 2.5×10^{10} to 1.34×10^{11} M$_\odot$, corresponding to a factor of $\simeq$5.4. Therefore, with our normalization of the black hole accretion rate in equation (3), the black hole mass to bulge mass ratio is comparable at the beginning and at the end. The observations suggest that the scatter in the black hole mass to bulge mass relation is small (see Section 1 and also Häring & Rix 2004). This means that our normalization of the black hole accretion rate is not far away from the appropriate value because it preserves the $M_\bullet/M_{\rm spheroid}$ ratio.

The star formation rate in the nuclear region closely follows the global star formation of the host galaxy. It has two peaks, which coincide with the first and second pericentre passages. Fig. 7

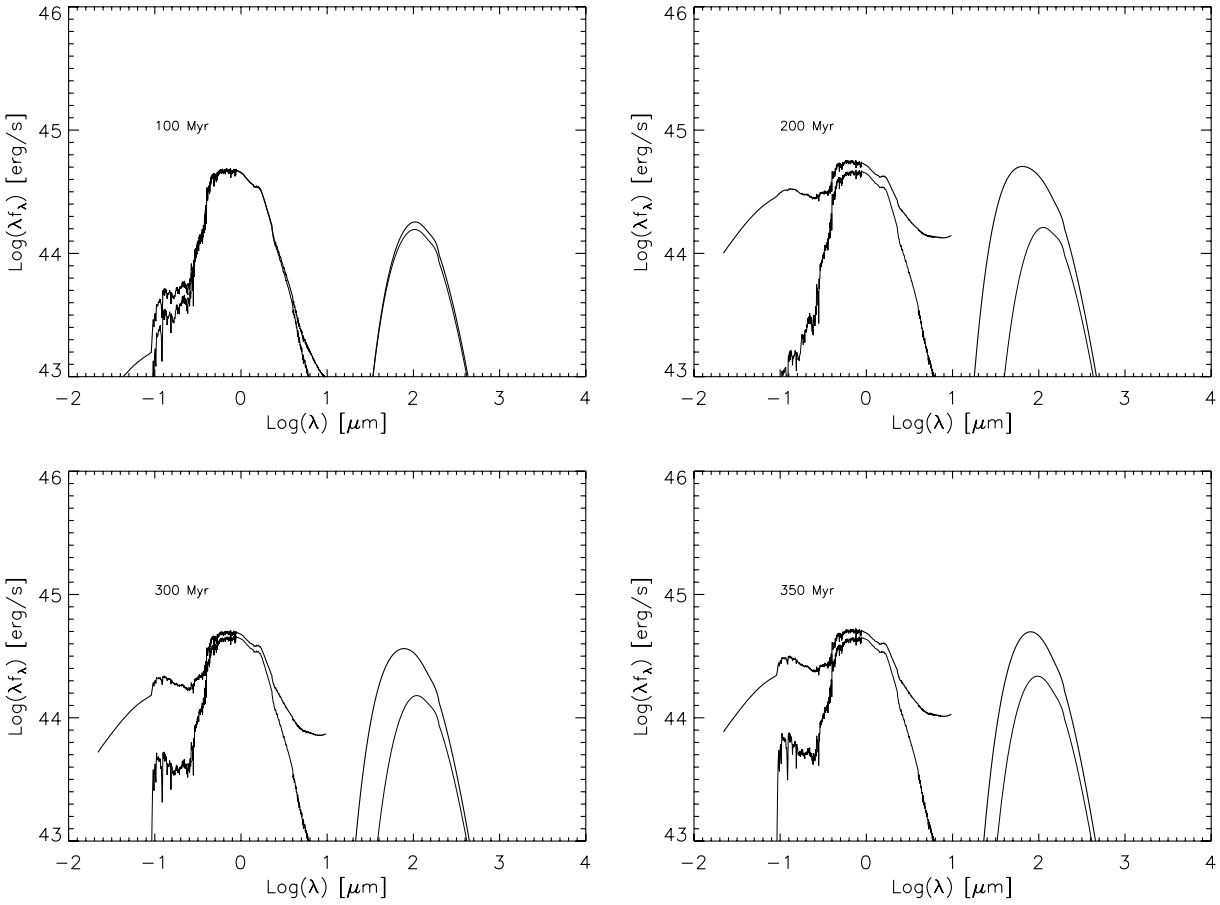

Figure 11. Global spectral energy distribution of the interacting system 100, 200, 300 and 350 Myr after the simulation has started. At optical wavelengths, the thick line (above) corresponds to the case in which in the AGN is visible and the thin line (below) to the case in which it is obscured. At IR wavelengths, the thick line (above) corresponds to dust heated by stars and by the AGN. The thin line (below) corresponds to dust heated by stars only.

compares the star formation in our merger simulation with the star formation rate in a simulation in which there is only one isolated galaxy. Manifestly, the dynamical instability deriving from the initial conditions for the discs, which are thin and axisymmetric, exaggerate the pace at which spiral arms form and gas fragments into knots. Nevertheless, we believe that the filamentary lumpiness of star formation evident in Fig. 5 reflects a real astrophysical phenomenon. Therefore, the first peak in Fig. 6 is artificial. Instead, the second peak is physical and corresponds to the actual merger. The starburst triggered by the merger is ∼6 times more intense than quiescent star formation. Its duration is of the order of 10 Myr. This peak coincides with maximum AGN activity and occurs when the merger remnant begins to look like a lenticular galaxy both colour-wise and morphology-wise (Fig. 4).

Young stars are concentrated in the nuclear starburst ring. Therefore, it is difficult to disentangle their light from the AGN point spread function (point sources appear to have spikes connected by a spider web owing to instrumental diffraction; see Fig. 10). However, this is a merger with a low gas fraction. It is possible that, in the case of a gas-rich merger, star formation is no longer confined to the nuclear region, but distributed throughout the host galaxy (Kauffmann et al. 2003).

We observe the formation of a dusty torus, which obscure the AGN from most viewing angles. The torus has an opening angle of $30^\circ - 40^\circ$ and its properties are consistent with expectations of unified model (see Rowan-Robinson 1995) if the torus is made of clouds with $n_{\rm H} \sim 10^{24}$ cm^{-2} (like the Orion nebula). Our model predicts that in some cases the AGN is obscured even from a face-on viewing angle owing to the presence of clouds in the polar regions, while, in other cases, we can still see the AGN from nearly equatorial viewing angles because there are holes in the dust distribution.

ACKNOWLEDGMENTS

AC acknowledges the support of the European Commission through a Marie Curie Research Fellowship. He also wishes to thank B. Guiderdoni and M. Rowan-Robinson for useful conversation, F. Durret for help with the IRAF software and G. Mamon for comments on the manuscript.

REFERENCES

Antonucci R. R. J., Miller J. S., 1985, ApJ, 297, 621
Aubert D., Pichon C., Colombi S., 2004, MNRAS, 352, 376
Barger A. J., Cowie L. L., Brandt W. N., Capak P., Garmire G. P., Hornschemeier A. E., Steffen A. T., Wehner E. H., 2002, AJ, 124, 1839
Barger A. J., Cowie L. L., Mushotzky R. F., Yaug Y., Waug W.-H., Steffeu A. T., Capak P., 2005, AJ, 129, 578
Barnes J. E., Hernquist L. E., 1991, ApJ, 370, L65
Barnes J. E., Hernquist L., 1996, ApJ, 471, 115
Binney J., Tremaine S., 1987, Galactic Dynamics. Princeton Univ. Press, Princeton, NJ, p. 747

Blumenthal G. R., Faber S. M., Primack J. R., Rees M. J., 1984, Nat, 311, 517
Brandt W. N. et al., 2001, AJ, 122, 2810
Bushouse H. A. et al., 2002, ApJS, 138, 1
Cattaneo A., 2001, MNRAS, 324, 128
Chokshi A., Turner E. L., 1992, MNRAS, 259, 421
Combes F., Melchior A. L., 2002, ApSS, 281, 383
Devriendt J. E. G., Guiderdoni B., Sadat R., 1999, A&A, 350, 381
Dunlop J. S., McLure R. J., Kukula M. J., Baum S. A., O'Dea C. P., Hughes D. H., 2003, MNRAS, 340, 1095
Fioc M., Rocca-Volmerange B., 1997, A&A, 326, 950
Häring N., Rix H., 2004, ApJ, 604, L89
Heller C. H., Shlosman I., 1994, ApJ, 424, 84
Hutchings J. B., Campbell B., 1983, Nat, 303, 584
Kauffmann G., Charlot S., 1998, MNRAS, 297, L23
Kauffmann G., Haehnelt M., 2000, MNRAS, 311, 576
Kauffmann G., White S. D. M., Guiderdoni B., 1993, MNRAS, 264, 201
Kauffmann G. et al., 2003, MNRAS, 346, 1055
Marconi A., Risaliti G., Gilli R., Hunt L. K., Maiolino R., Salvati M., 2004, MNRAS, 351, 169
Mihos J. C., Hernquist L., 1994, ApJ, 425, L13
Mihos J. C., Hernquist L., 1996, ApJ, 464, 641
Miyamoto M., Nagai R., 1975, PASJ, 27, 533
Rowan-Robinson M., 1995, MNRAS, 272, 737
Sazonov S. Y., Ostriker J. P., Sunyaev R. A., 2004, MNRAS, 347, 144
Searle L., Sargent W. L. W., Bagnuolo W. G., 1973, ApJ, 179, 427
Segalovitz A., 1975, A&A, 40, 401
Shlosman I., Noguchi M., 1993, ApJ, 414, 474
Soltan A., 1982, MNRAS, 200, 115
Toomre A., Toomre J., 1972, ApJ, 178, 623
Ueda Y., Akiyama M., Ohta K., Miyaji T., 2003, Astron. Nachr., 324, 36
Xilouris E. M., Papadakis I. E., 2002, A&A, 387, 441
Yu Q., Tremaine S., 2002, MNRAS, 335, 965

This paper has been typeset from a TEX/LATEX file prepared by the author.